Internal stresses in TiN/Ti multilayer coatings deposited by large area filtered arc deposition

Y. H. Cheng,[1,a)] T. Browne,[1] B. Heckerman,[1] J. C. Jiang,[2] E. I. Meletis,[2] C. Bowman,[3] and V. Gorokhovsky[3]
[1]*American Eagle Instruments, Inc., 6575 Butler Creek Rd., Missoula, Montana 59808, USA*
[2]*Materials Science and Engineering Department, University of Texas at Arlington, Arlington, Texas 76019, USA*
[3]*Arcomac Surface Engineering, LLC, 151 Evergreen Dr., Suite D, Bozeman, Montana 59715, USA*

(Received 25 July 2008; accepted 9 September 2008; published online 4 November 2008)

A series of TiN/Ti multilayer coatings with fixed TiN layer thickness and different Ti layer thicknesses were deposited using a large area filtered arc deposition technique. X-ray diffraction was used to investigate the crystalline structure, lattice strain, and crystallinity of the deposited coatings. A substrate curvature method was used to measure the internal stress in the multilayer coatings. The influence of the Ti interlayer thickness on the crystalline structure and internal stress in the coatings was systematically studied. It was found that a cubic TiN phase and hexagonal Ti phase exist in all the multilayer coatings. The TiN and Ti layers in the multilayer coatings exhibit a strong (111) and (002) preferred orientation, respectively. With the increase in the Ti layer thickness, the *d*-spacing decreases and the peak width increases for both TiN (111) and Ti (002) peaks, indicating a decrease in the lattice strain and an increase in the crystallinity of both TiN and Ti phases. It is suggested, that the reduction in the defect density in both TiN and Ti layers and the relaxation of the stain by the diffusion of the Ti atoms in the underneath Ti layer contribute to the decrease in the total internal stress with increasing Ti layer thickness. © *2008 American Institute of Physics*.
[DOI: 10.1063/1.3006136]

I. INTRODUCTION

Transition nitride coatings have been widely used in the mechanical, aerospace, and medical industries to protect tools and components/parts due to their high hardness, excellent wear resistance, and corrosion resistance.[1–3] However, the high internal stress formed during coating deposition and the brittle nature of the ceramic nitride coatings limit the coating thickness and their service life.[4–9] Incorporation of metallic interlayers into the ceramic coatings is an effective way to reduce the internal stress and improve toughness.[4,8]

Due to the high ion energy and high ionization rate, cathodic arc was routinely used in the industry to deposit hard nitride coatings for machine tools and mechanical parts. However, the macroparticles formed during the cathodic arc evaporation degrade the coating properties, especially the corrosion and wear resistance. Our patented large area filtered cathodic arc deposition (LAFAD) technique uses a filtered cathodic arc source;[10–15] utilizing 90° deflecting magnetic fields to deflect ions from the cathodic arc plasma to the deposition chamber and remove the unwanted macroparticles generated during arc evaporation. When the deflecting magnetic fields are turned on, the filtered cathodic arc source provides a fully ionized flow of target metal vapor with a high concentration of dissociated, ionized, and activated reactive gas. Extremely high ion currents are obtained with the metal ion species, with ionization efficiencies approaching nearly 100%. The LAFAD source provides an ion current of up to 4 A, which translates into an ion current density of $5\ \mathrm{mA/cm^2}$ for a source with a window of $20\times 40\ \mathrm{cm^2}$. This capability results in a highly productive deposition process. By manipulating the arc plasma jets using strategically placed scanning magnetic coils and auxiliary anodes, this novel design creates a "plasma-immersion" environment in the coating chamber. This design substantially reduces the shadowing effect that causes nonuniform coating thickness when complex, three-dimensionally shaped substrates are coated in conventional deposition systems.

In this study, Ti interlayers were introduced into the TiN coatings to reduce the internal stress of the ceramic nitride coatings. A series of TiN/Ti multilayer coatings with fixed TiN layer thickness and different Ti layer thicknesses were deposited using our LAFAD technique. The influence of the Ti interlayer thickness on the crystalline structure and internal stress of both TiN and Ti interlayer as well as the total internal stress of the multilayer coatings was systematically studied.

II. EXPERIMENT

A LAFAD-1 surface engineering system, as shown in Fig. 1, was used to perform TiN/Ti multilayer coating deposition. This system includes one dual filtered arc source, one rectangular plasma-guide chamber, one deposition chamber, auxiliary anode and heating system, substrate bias system, and vacuum system. The dual filtered arc source consists of two primary cathodic arc sources utilizing round Ti targets, which are placed opposite to each other on the sidewalls of the plasma-guide chamber, surrounded by rectangular de-

[a)]Author to whom correspondence should be addresses. Electronic addresses: yh_cheng@yahoo.com and ycheng@am-eagle.com.

 © 2008 American Institute of Physics

Downloaded 04 Nov 2008 to 153.90.6.19. Redistribution subject to ASCE license or copyright; see http://jap.aip.org/jap/copyright.jsp

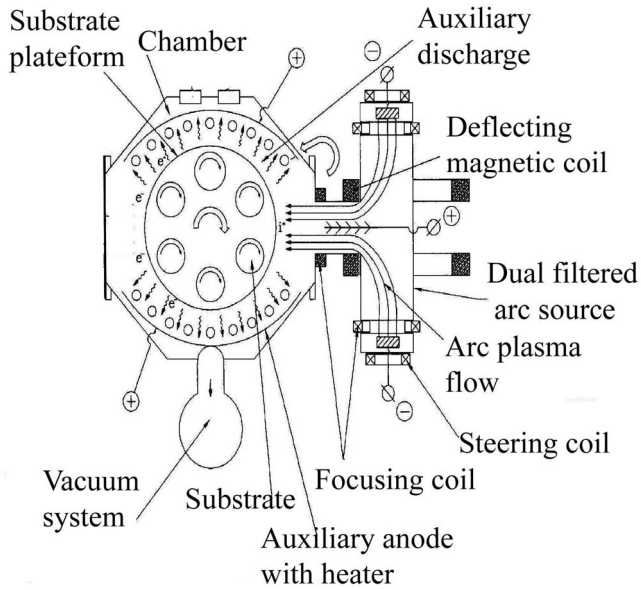

FIG. 1. LAFAD surface engineering system.

flecting coils, and separated by an anodic baffle plate. Two rectangular deflecting coils installed on the opposite sides of the rectangular plasma-guide chamber were used to turn the metal ion flow 90° toward the deposition chamber. The ion flow can be swept by a set of scanning magnetic coils in the vertical direction to cover theoretically unlimited large surface areas. At the same time, the arc column is well confined by a magnetic field in the horizontal direction, providing enhanced suppression of the turbulent plasma diffusion, leading to a significant increase in the metal vapor ion yield. The deposition temperature was controlled by heating elements. The deposition zone for this system is about 50 cm diameter $\times$ 30 cm high. 17–4 stainless coupons and 5 cm *n*-type (111) Si wafers with a resistivity and thickness of $<0.005\ \Omega$ cm and $279 \pm 25\ \mu$m, respectively, were used as substrates for characterizing the crystalline structure and internal stress in the coatings, respectively. 17–4 stainless steel coupons were cut from $\phi 12.5 \times 30\ \text{cm}^2$ bars, followed by grinding and polishing to a mirror finish surface. In each run, six steel coupons and one Si wafer were loaded into the deposition chamber and coated with multilayer coating.

The substrates were thoroughly cleaned and dried using an ultrasonic cleaning system prior to loading into the deposition chamber. Before deposition, the coupons were subjected to Ar plasma cleaning at 0.08 Pa pressure, 350 °C temperature, −250 V bias for 15 min Ti ion subimplantation followed at 0.02 Pa pressure, 500 V bias for 2 min. In order to improve the adhesion of the ceramic TiN/Ti multilayer, a Ti–TiN gradient multilayer was deposited onto the coupon surface. The detailed deposition process for the gradient multilayer is shown in Table I.

A series of TiN/Ti coatings with fixed TiN layer thickness and different Ti layer thicknesses were designed to investigate the influence of the Ti layer thickness on the crystalline structure and internal stress. The thicknesses of the TiN layer and the entire TiN/Ti multilayer coatings were set to 240 nm and 3 μm, respectively. The Ti sublayer thickness was designed to be 0, 25, 50, 100, and 150 nm, which was

TABLE I. Deposition process for the Ti–TiN gradient layer.

Step	Gas	Bias (−V)	Temperature (°C)	Pressure (Pa)	Time (min)
1	100%Ar	80	350	0.02	10
2	85%Ar+25%N2	40	350	0.02	5
3	50%Ar+50%N2	40	350	0.02	5
4	25%Ar+75%N2	40	350	0.02	5

controlled by varying the deposition time. The detailed deposition parameters for TiN and Ti sublayers are shown in Table II. The deposition rate was measured by measuring the coating thickness and deposition time, and was controlled by adjusting the deposition time. The deposition temperature was measured by a thermal couple attached to the top of the deposition chamber, and was controlled by a proportional-integral derivative controller.

The phase structure and grain size of the TiN/Ti multilayer coated samples were studied using a Siemens D500 x-ray diffractometer with a Cu $K\alpha$ radiation source ($\lambda = 0.15406$ nm). The accelerating voltage and filament current were 40 kV and 30 mA, respectively.

The in plane internal stress in the as-deposited TiN/Ti multilayer coatings was determined by the radius of curvature technique which compares the curvatures of the bare silicon substrates and substrates coated with a film. The stress component perpendicular to the film surface is negligible because the film is free to expand or contract in this direction. The stress was given by Stoney's equation,[9]

$$\sigma = \frac{E_s t_s^2}{6(1-\nu_s)t_c}\left(\frac{1}{R_a} - \frac{1}{R_b}\right),$$

where E_s and ν_s are Young's modulus and Poisson's ratio for the substrate, t_s and t_c are the thicknesses of the substrate and coating, R_a and R_b are the spherical radii of curvature of the substrate after and before coating deposition, respectively.

The radius of the curvature of the Si wafer was measured by a contact skidless type surface profilometer (Veeco Dektak8). The stylus radius, stylus force, and scan length were set to 5 μm, 10 mg, and 25 mm, respectively. Before and after coating deposition, the radius of curvature of each Si wafer was measured at exactly the same location close to the wafer center. For each wafer, three measurements were conducted and their average is reported.

The coating thickness was measured using a Calotester (CSM). During testing, a 52100 steel ball (grade 5) with a diameter of 0.75 in. was rotating against the coating surface. Diamond slurry with a particle size of 0.5–1 μm was used to create a wear scar, which was polished using diamond

TABLE II. Deposition process for the TiN/Ti multiplayer.

Layer	Gas	Bias (−V)	Temperature (°C)	Pressure (Pa)	Deposition rate (nm/min)
TiN	100%N_2	40	350	0.02	12.5
Ti	100%Ar	40	350	0.02	12.5

Downloaded 04 Nov 2008 to 153.90.6.19. Redistribution subject to ASCE license or copyright; see http://jap.aip.org/jap/copyright.jsp

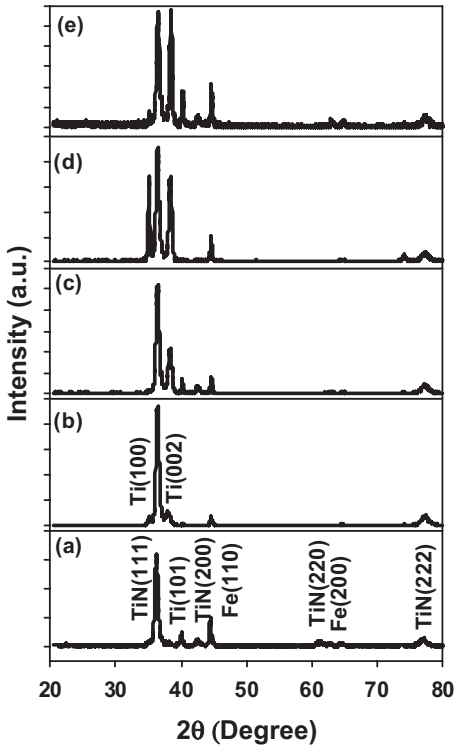

FIG. 2. XRD patterns of the TiN/Ti multilayer coatings with Ti interlayer thickness of (a) 0, (b) 25, (c) 50, (d) 100, and (e) 150 nm on stainless steel substrate.

slurry with a particle size of 0–0.2 μm. The following equation was used to calculate the coating thickness:

$$t_c = \frac{1}{2}(\sqrt{4R^2 - d^2} - \sqrt{4R^2 - D^2}),$$

where R is the radius of the steel ball and d and D are the diameters of the inner and outer circles of the coating wear scar, respectively.

III. RESULTS AND DISCUSSION

To identify the phase structure of the TiN/Ti multilayer, x-ray diffraction (XRD) measurements were conducted in the 2θ range of 20°–80° with a θ-2θ scan. Coatings on both Si and stainless steel substrates were characterized using XRD, and showed similar crystalline structure. Figure 2 shows the typical XRD patterns of the TiN/Ti multilayer coatings with a Ti layer thickness of (a) 0, (b) 25, (c) 50, (d) 100, and (e) 150 nm, on stainless steel substrates. For the coating with a Ti layer thickness of 0 nm (pure TiN coating), seven peaks can be observed at 2θ angles of 36.18°, 40.12°, 42.55°, 44.46°, 60.96°, 62.95°, and 77.04°. After comparing with the XRD spectra of the steel substrate, it can be found that the fourth and sixth peaks are from the steel substrate and correspond to the (110) and (200) planes of α-Fe. According to Ref. 16, the first, third, fifth, and seventh peaks correspond to the (111), (200), (220), and (222) planes of the TiN phase, indicating that the deposited coatings are a stoichiometric TiN coating. The intensity ratio of the TiN (111) peak to the (200) peak is calculated to be 18.5, which is extremely higher than the ratio, 0.71, from randomly oriented polycrystalline powder. This indicates that the deposited TiN coatings exhibit strong (111) preferred orientation.

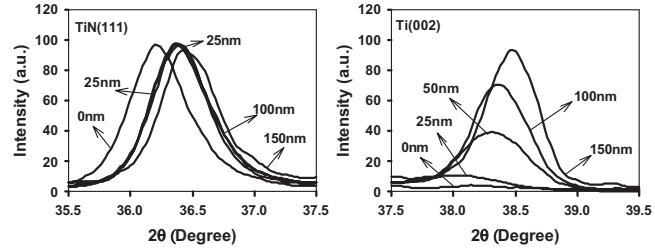

FIG. 3. TiN (111) and Ti (002) peak of different TiN/Ti multilayer coatings with different Ti layer thickness on stainless steel substrate.

It is typical for coatings deposited by physical vapor deposition to exhibit preferred orientation.[17–20] It is well accepted now that the preferred orientation of the coating is controlled by the strain energy and surface energy of the specific crystalline orientation of the coatings. The (111) plane in the TiN crystal has the lowest strain energy,[20] while the (200) plane has the lowest surface energy. It is assumed that the growing coating develops a crystallographic texture in order to minimize its total energy. For the current TiN/Ti multilayer coatings, the existence of the high internal stress, as discussed below, generates high strain energy in the coatings. To minimize the total energy, the coatings tend to grow with the (111) plane parallel to the surface due to its low strain energy. This contributes to the strong (111) preferred orientation of the TiN/Ti multilayer coatings deposited by LAFAD technique.

The second peak corresponds to the (101) plan of the Ti phase with a hexagonal structure. The Ti phase is believed to result from the Ti bonding layer between the TiN coating and the steel substrate. According to Ref. 21, the Ti (101) peak possesses the highest intensity, indicating that the Ti layer does not have preferred orientation. XRD pattern shows that no other phases exist in the coating.

For the XRD pattern from TiN/Ti multilayer coatings with Ti layer thickness of 25 nm, Fig. 2(b), the Ti (101) peak disappears, but two additional weak peaks at 2θ angles of 35.09° and 38.08°, corresponding to the (100) and (002) planes of Ti phase, respectively, can be distinguished. The high intensity ratio of the (100) and (002) peak to that of the (101) peak indicates the Ti layer exhibits (100) and (002) preferred orientation. The weak feature of these two peaks implies small grain size and high defect density in the Ti layer.

With the increase in the Ti sublayer thickness to 50 nm, a rapid increase in the relative intensity of the Ti (002) peak to the TiN (111) peak and a narrowing of the Ti (002) peak can be clearly observed, indicating an increase in the Ti phase content as well as the crystallinity of the Ti sublayer. The further increase in the Ti layer thickness results in a continuous increase in the relative intensity of the Ti (002) peak to the TiN (111) peak.

Figure 3 illustrates the XRD patterns of the TiN/Ti multilayer coatings on stainless steel substrate at 2θ angle ranges of (a) 35.5°–37.5°, and (b) 37.5°–39.5°. For the ease of comparison, the TiN (111) peak intensity was normalized to 100. It is interesting to note that the TiN (111)

Downloaded 04 Nov 2008 to 153.90.6.19. Redistribution subject to ASCE license or copyright; see http://jap.aip.org/jap/copyright.jsp

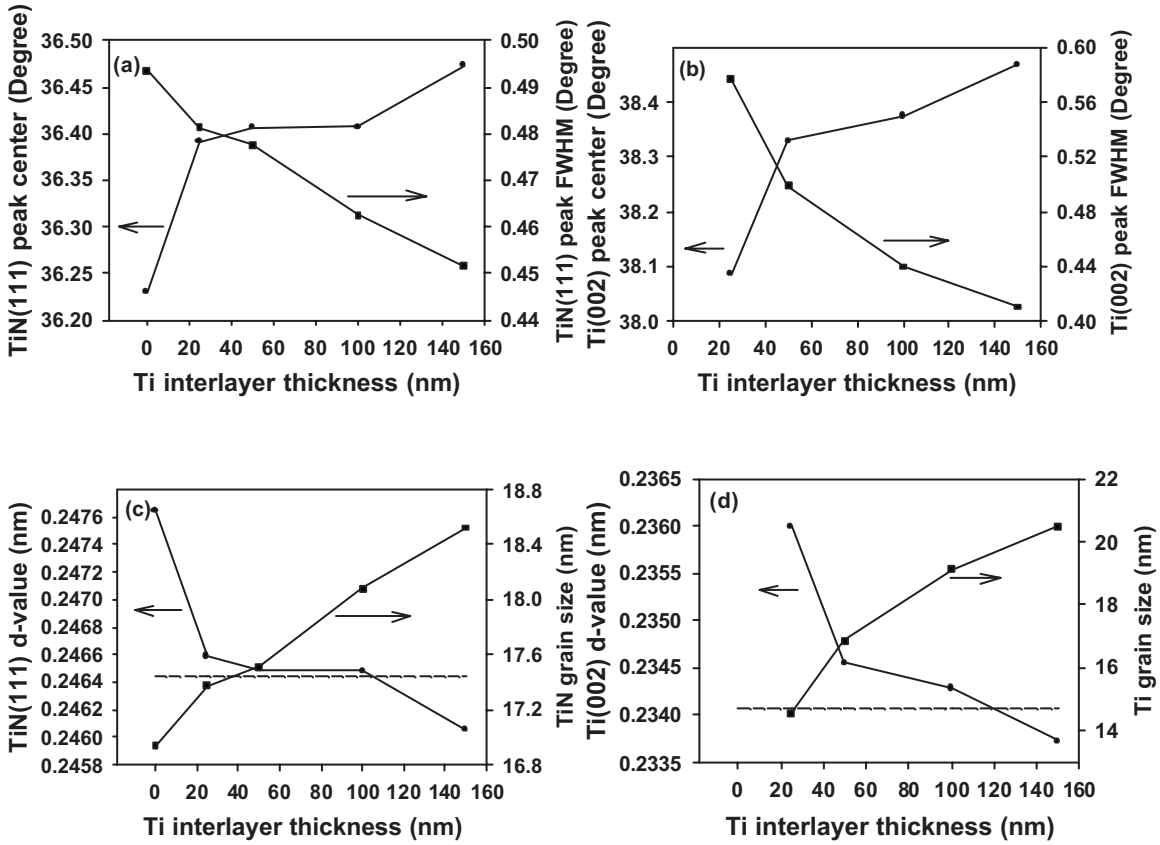

FIG. 4. Dependence of the peak center and FWHM of the (a) TiN (111) and (b) Ti (002) XRD peak on the Ti layer thickness, and the dependence of the calculated (c) TiN (111) *d*-spacing values and TiN grain size and (d) Ti (002) *d*-spacing values and Ti grain size on the Ti layer thickness.

peak center shifts to a higher 2θ angle with increasing Ti layer thickness. For the Ti (002) peak, a dramatic increase in the intensity and a shift of the peak center to a higher 2θ angle with increasing Ti layer thickness can be observed.

To quantify the change in the peak center and width with Ti layer thickness, the TiN (111) and Ti (002) peaks of the TiN/Ti multilayer coatings were fitted using a Gaussian function. The fitted peak center and full width at half maximum (FWHM) of the TiN (111) peak and the Ti (002) peak are shown in Figs. 4(a) and 4(b), respectively. As shown in Fig. 4(a), the FWHM of the TiN(111) peak decreases linearly with increasing Ti layer thickness, indicating a continuous increase in the grain size and crystallinity of the TiN phase in the multilayer coatings. However, the TiN (111) peak center shifts significantly from 36.23° to 36.39°, after adding a very thin Ti layer (50 nm) to the TiN coatings. The further increase in the Ti layer thickness to 150 nm results in a gradual increase in the 2θ angle of the TiN (111) peak center to 36.47°. For the Ti(002) peak, a similar variation trend can be observed. The FWHM of the Ti (002) peak decreases with increasing Ti layer thickness, indicating an increase in the grain size and crystallinity of the Ti phase. The Ti (002) peak center shifts significantly from 38.08 to 38.33 with the increase in the Ti layer thickness from 25 to 50 nm. Further increase in the Ti layer thickness to 150 nm results in a gradual increase in the 2θ angle of the Ti (002) peak center to 38.47°.

Figures 4(c) and 4(d) display the interplanar spacing values (*d*-value) and grain size of the TiN (111) plane and the Ti (002) plane, respectively, of the TiN/Ti multilayer coatings as a function of the Ti layer thickness. The *d*-values for the TiN (111) and the Ti (002) planes were calculated using Bragg's law, $1/d_{hkl}=(2/\lambda)\sin\theta$, where d_{hkl}, λ, and θ are interplanar spacing of the (hkl) plane, wavelength of the x ray, and half of the diffraction angle, respectively. The grain size was computed using the Scherer equation[22]

$$D = \frac{0.9\lambda}{B\cos\theta},$$

where D is the diameter of the grain, B is the FWHM of the diffraction peak, and θ is half of the diffraction angle.

It can be seen that the grain size for both TiN and Ti crystallites increases linearly with increasing Ti interlayer thickness. With increasing Ti interlayer thickness from 0 to 150 nm, the TiN grain size increases slightly from 16.9 to 18.5 nm, but Ti grain size increases remarkably from 14.5 to 20.5 nm. It is well known that the growth of crystallites in the coatings involves two processes: nucleation and growth processes. For the Ti layer with small thickness, the growth process of the Ti nuclei was stopped by the subsequent TiN layer deposition, which limits the Ti grain size. The increase in the Ti layer thickness corresponds to a longer deposition time, enabling the further growth of the Ti grain, and therefore the increase in the Ti grain size. The increase in the TiN grain size with increasing Ti layer thickness is believed to

Downloaded 04 Nov 2008 to 153.90.6.19. Redistribution subject to ASCE license or copyright; see http://jap.aip.org/jap/copyright.jsp

result from the larger grain size of the underlying Ti layer, which acts as a template for the succeeding TiN layer deposition.

The dotted line in the graph is the interplanar spacing of the TiN (111) and Ti (002) planes obtained from the JCPDS standard cards. It is interesting to note that the d-spacing values of both planes for the TiN/Ti multilayer coatings are larger than the value from JCPDS cards except for the coatings with a Ti layer thickness of 150 nm, which shows reduced d-spacing values.

When the x-ray diffractometer was operated in the θ-2θ scan mode, the residual stress in the coating can be calculated quantitatively using the equation[23]

$$\sigma = -\frac{E}{\nu}\left(\frac{d_n - d_0}{d_0}\right),$$

where E, ν, d_n, and d_0 are Young's modulus, Poisson's ratio of the coatings, d-spacing value of the diffraction plane parallel to the surface of the coating under stress, and the d-spacing value of the same series of planes in the stress-free condition, respectively. As it is impossible to measure d_0 in the θ-2θ scan mode, we cannot directly calculate the internal stress in the deposited coatings. Although the d_0 is strongly dependent on the coating composition, structure, and crystallinity, the d_0 from the PDF file could be used as a reference. The larger d-spacing values for the Ti (111) and Ti (002) planes in the TiN/Ti multilayer coatings indicate that the stresses in both TiN and Ti layer are compressive.

By comparing the d-spacing values of the Ti (111) plane for different TiN/Ti multilayer coatings, it can be seen that adding a very thin Ti interlayer to the TiN coatings leads to a significant decrease in the d-spacing values, indicating a great reduction in the internal stress in the TiN layer. Further increase in the Ti layer thickness leads to a slight decrease in the d-spacing values. For the Ti (002) plane, the increase of the Ti layer thickness from 25 to 50 nm results in a significant decrease in the d-spacing values, indicating a considerable decrease in the internal stress in the Ti layer. A further increase in the Ti layer thickness results in a gradual decrease in the Ti (002) d-spacing values, indicating a gradual decrease in the internal stress in the Ti layer.

To quantitatively ascertain the change of the internal stress with Ti layer thickness, a curvature method was used to measure the total internal stress in the TiN/Ti multilayer coatings. In order to obtain more accurate results, very thin and electrical conductive Si wafers were selected. The radius of the Si wafers was measured before and after coating deposition. Figure 5 shows the surface profiles of the Si wafers before and after TiN/Ti multilayer coating deposition. As shown, all Si wafers exhibit a very small radius before coating deposition, but a significant increase in the radius can be seen after deposition, indicating the existence of a compressive stress in all the deposited coatings. Before coating deposition, the radius of the Si wafers is only 1%–5% of the radius of the wafers after coating deposition. In addition, we can observe that the Si wafer with TiN coatings shows the largest radius; and the increase in the Ti layer thickness results in a continuous decrease in the radius, indicating a continuous decrease in the internal stress in the deposited coatings.

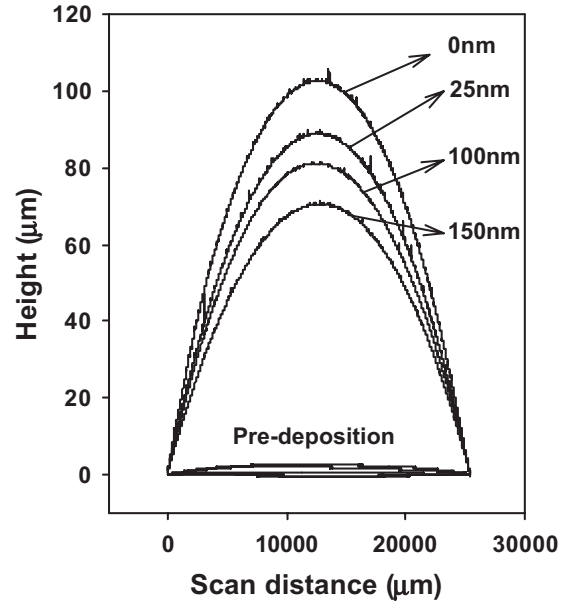

FIG. 5. Surface profiles of Si wafers before and after TiN/Ti multilayer coating deposition with different Ti layer thickness.

The calculated internal stress in the TiN/Ti multilayer coatings as a function of the Ti layer thickness is plotted in Fig. 6. The internal stresses in all the TiN/Ti multilayer coatings are compressive. The increase in the Ti layer thickness from 0 to 25 nm leads to a rapid decrease in the internal stress from 2.2 to 1.6 GPa, which decreases continuously to 0.88 GPa with further increase in the Ti layer thickness to 150 nm. Interestingly, the variation trend of the internal stress with Ti layer thickness is in excellent agreement with that of the Ti (111) d-spacing values with Ti layer thickness in Fig. 4(c), indicating that the XRD is a convenient way of qualitatively evaluating the internal stress in the coatings. The hardness of the TiN/Ti multilayer coatings were also measured using nanoindentation technology. The effective hardness and Young's modulus of the TiN/Ti coatings decreases linearly from 32 and 330 GPa to 20 and 300 GPa, respectively, with increasing Ti layer thickness from 0 to 50 nm, followed by a gradual decrease to 16 and 240 GPa, respectively, with increasing Ti layer thickness to 150 nm.

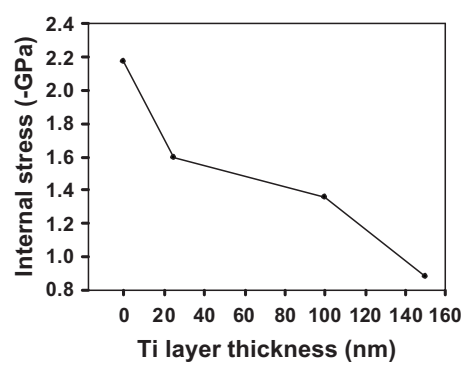

FIG. 6. Dependence of the internal stress of TiN/Ti multilayer on the Ti layer thickness.

Downloaded 04 Nov 2008 to 153.90.6.19. Redistribution subject to ASCE license or copyright; see http://jap.aip.org/jap/copyright.jsp

It is recognized now that the internal stress is one of the most important properties of the coatings because it affects the adhesion and long-term integrity of the coatings during service. The total internal stress (σ_{tot}) in the coatings originates from thermal (σ_{th}) and intrinsic (σ_{int}) stress.[24] The thermal stress component originates mainly from the differences in the thermal expansion coefficient between the film and substrate. In the current study, as the deposition temperature is the same for all coatings, the influence of the thermal stress on the change in the total internal stress in the coatings is negligible.

It has been well accepted that the intrinsic compressive stresses in the coatings originate from the "atomic peening" mechanism.[25–29] For cathodic arc, the energy of Ti ions that reach the substrate surface can be estimated as $E_{Ti}=E_0-qV_b$, where E_0 is the energy of Ti ions emitted from arc sources, q is the mean charge state of Ti ions, and V_b is the applied substrate bias. The E_0 and q of Ti ions have been measured to be 76 eV and 1.79, respectively.[30] In this study, the substrate bias for all coatings remained at −40 V. The energy of Ti ion that reaches the coating surface is estimated to be 147.6 eV, which is sufficiently high enough to subplant the Ti ions into the subsurface of the growing coatings, as well as for knocking the surface atoms into the subsurface. Due to the low mobility of the atoms in the coatings, these subplanted or knocked atoms can be trapped in the subsurface, leading to an expansion of the film outwards from the substrate. However, the coatings are confined by the substrate, corresponding to the outward bending of the Si substrate, as shown in Fig. 5. The highly strained substrate will exert an opposite compressive stress to the deposited coatings.

For TiN/Ti multilayer coatings, during the deposition of the ceramic layer, highly compressive stress will form in the layer, which exerts high tensile stress to the underlying Ti layer, facilitating the diffusion and migration of the Ti atoms in the Ti layer. This process releases the strain formed in the TiN and Ti layer, and therefore, the reduction in the internal stress in the TiN and Ti layer, as shown in Fig. 4.[31–34] This also explains why adding a very thin Ti layer, 25 nm, into the TiN results in a 27% decrease in the internal stress, as shown in Fig. 6. In addition, the narrowing of the Ti (111) XRD peaks with increasing the Ti layer thickness indicates the decrease in the defect and distortion in the TiN lattice. It is well known that the defect and distortion in the lattice generate strain in crystalline materials.[35] The decrease in the defect and distortion also contributes to the decrease in the internal stress in the TiN layer.

For a thin Ti layer, the broad feature of the XRD patterns indicates the existence of a large quantity of defects and distortion in the lattice, which corresponds to the presence of high internal stress. With the increase of the Ti layer thickness, the FWHM of the Ti XRD peaks decreases significantly, indicating the reduction in the defect density and the distortion of the Ti lattice, corresponding to the continuous decrease in the stress in the Ti layer. The decrease in the internal stress in both TiN and Ti layer with increasing Ti layer thickness contributes to the decrease in the total internal stress in the multilayer coatings.

In addition, for metallic coatings, due to the nature of the metallic bonding, the atoms in the coatings have higher mobility, which can release part of the strain caused by the atomic peening effect, corresponding to the low internal stress in the Ti layers as compared to that in the nitride layers. As the total thickness of the TiN/Ti coatings is the same, the increase in the Ti layer thickness results in a decrease in the TiN layer thickness. This also corresponds to the continuous decrease in the total internal stress in the coatings with increasing Ti layer thickness.

IV. CONCLUSIONS

In this study, a LAFAD deposition technique was used to deposit TiN/Ti multilayer coatings with fixed TiN layer thickness and varying the Ti layer thickness to investigate its influence on the crystalline structure and internal stress of the coatings. XRD results show that the TiN/Ti multilayer coatings consist of cubic TiN phase and hexagonal Ti phase. The TiN and Ti layer in the multilayer coatings exhibit a strong preferred (111) and (002) orientation, respectively. The increase in the Ti layer thickness results in a decrease in the internal stress in both the TiN and Ti layers, and an increase in the grain size and crystallinity of both TiN and Ti phases. Internal stress results, measured by substrate curvature method, confirm the decrease in the total internal stress in the coatings with increasing Ti layer thickness.

ACKNOWLEDGMENTS

The authors would like to express gratitude for the support of The United States Army Telemedicine and Advanced Technology Research Center (TATRC), U.S. Army Medical Research and Material Command under Contract No. W81XWH-08-2-0023.

[1] E. I. Meletis, W. B. Carter, and R. F. Hochman, Microstruct. Sci. **13**, 417 (1984).
[2] C. Mitterer, F. Holler, F. Ustel, and D. Heim, Surf. Coat. Technol. **125**, 233 (2000).
[3] R. Wei, J. J. Vajo, J. N. Matossian, and M. N. Gardos, Surf. Coat. Technol. **158–159**, 465 (2002).
[4] E. Bemporad, M. Sebastiani, C. Pecchio, and S. De Rossi, Surf. Coat. Technol. **201**, 2155 (2006).
[5] A. G. Evans and J. W. Hutchinson, Surf. Coat. Technol. **201**, 7905 (2007).
[6] F. R. Lamastra, F. Leonardi, R. Montanari, F. Casadei, T. Valente, and G. Gusmano, Surf. Coat. Technol. **200**, 6172 (2006).
[7] M. Gelfi, G. M. La Vecchia, N. Lecis, and S. Troglio, Surf. Coat. Technol. **192**, 263 (2005).
[8] T. Mori, S. Fukuda, and Y. Takemura, Surf. Coat. Technol. **140**, 122 (2001).
[9] A. Mezin, Surf. Coat. Technol. **200**, 5259 (2006).
[10] V. I. Gorokhovsky, V. P. Polistchook, and I. M. Yartsev, Surf. Coat. Technol. **61**, 101 (1993).
[11] Z. Has, S. Mitura, and V. Gorokhovsky, Surf. Coat. Technol. **47**, 106 (1991).
[12] V. I. Gorokhovsky, Surf. Coat. Technol. **61**, 108 (1993).
[13] V. I. Gorokhovsky, D. G. Bhat, and R. Bhattacharya, Surf. Coat. Technol. **140**, 215 (2001).
[14] V. I. Gorokhovsky, R. Bhattacharya, and D. G. Bhat, Surf. Coat. Technol. **140**, 82 (2001).
[15] V.Gorokhovsky, U.S. Patent No. 6,663,755 (2003).
[16] JCPDS Card No. 65-0965.
[17] Y. H. Cheng and B. K. Tay, J. Cryst. Growth **252**, 257 (2003).
[18] J. E. Greene, J.-E. Sundgren, L. Hultman, I. Petrov, and D. B. Bergstrom, Appl. Phys. Lett. **67**, 2928 (1995).

Downloaded 04 Nov 2008 to 153.90.6.19. Redistribution subject to ASCE license or copyright; see http://jap.aip.org/jap/copyright.jsp

[19]J. P. Zhao, X. Wang, T. S. Shi, and X. H. Liu, J. Appl. Phys. **79**, 9399 (1996).
[20]J. Pelleg, L. Z. Zevin, S. Lungo, and N. Croitoru, Thin Solid Films **197**, 117 (1991).
[21]JCPDS Card No. 65-3362.
[22]H. P. Klug and L. E. Alexander, *X-Ray Diffraction Procedures for Polycrystalline and Amorphous Materials* (Wiley, New York, 1974).
[23]L. V. Azaroff, *Elements of X-Ray Crystallography* (McGraw-Hill, New York, 1968).
[24]A. R. Zanatta and F. A. Ferri, J. Appl. Phys. **102**, 043509 (2007).
[25]F. M. d'Heurle, Metall. Trans. **1**, 725 (1970).
[26]C. A. Davis, Thin Solid Films **226**, 30 (1993).
[27]D. W. Hoffman and J. A. Thornton, Thin Solid Films **45**, 387 (1977).
[28]Y. H. Cheng, B. K. Tay, and S. P. Lau, J. Vac. Sci. Technol. A **20**, 1270 (2002).
[29]Y. H. Cheng, B. K. Tay, and S. P. Lau, J. Vac. Sci. Technol. A **19**, 557 (2001).
[30]R. L. Boxman, D. M. Sanders, P. J. Martin, and J. M. Lafferty, *Handbook of Vacuum Arc Science and Technology: Fundamentals and Applications* (Noyes, Park Ridge, NJ, 1995).
[31]G. Thornell, F. Ericson, and C. Hedlund, IEEE Trans. Ultrason. Ferroelectr. Freq. Control **46**, 981 (1999).
[32]P. Argyrakis, P. McNabb, A. J. Snell, and R. Cheung, Appl. Phys. Lett. **89**, 034101 (2006).
[33]H. T. Bekman, K. W. Benoist, and J. L. Joppe, Appl. Surf. Sci. **70**, 347 (1993).
[34]D. Gupta, *Diffusion Processes in Advanced Technological Materials* (William Andrew, New York, 2005).
[35]J.-D. Kamminga, Th. H. de Keijser, R. Delhez, and E. J. Mittemeijer, J. Appl. Phys. **88**, 6332 (2000).

Downloaded 04 Nov 2008 to 153.90.6.19. Redistribution subject to ASCE license or copyright; see http://jap.aip.org/jap/copyright.jsp